Science Advances
AAAS

advances.sciencemag.org/cgi/content/full/6/41/eabc0382/DC1

Supplementary Materials for

Self-regulated hirudin delivery for anticoagulant therapy

Xiao Xu, Xuechao Huang, Ying Zhang, Shiyang Shen, Zhizi Feng, He Dong, Can Zhang, Ran Mo*

*Corresponding author. Email: rmo@cpu.edu.cn

Published 9 October 2020, *Sci. Adv.* **6**, eabc0382 (2020)
DOI: 10.1126/sciadv.abc0382

This PDF file includes:

Figs. S1 to S16
Table S1

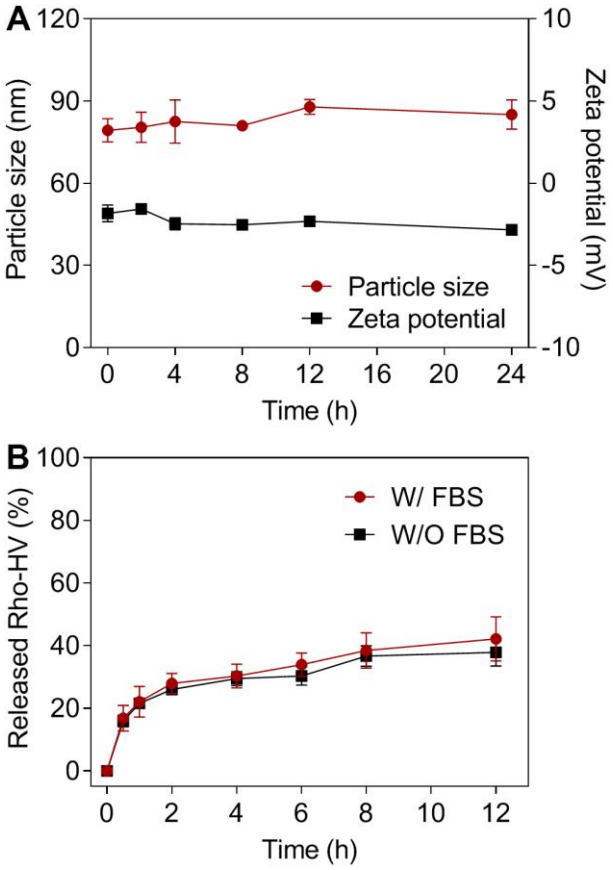

Fig. S1. *In vitro* stability of HV/ctNGs against serum proteins. (**A**) Changes in particle size and zeta potential of HV/ctNGs in the presence of BSA. HV/ctNGs were incubated with BSA (0.5%, w:v) at 37 ºC over time. Data are shown as mean ± s.d. (n = 3). (**B**) Release profiles of Rho-HV from Rho-HV/ctNGs after incubation with FBS (50%, v:v) over time. Data are shown as mean ± s.d. (n = 3).

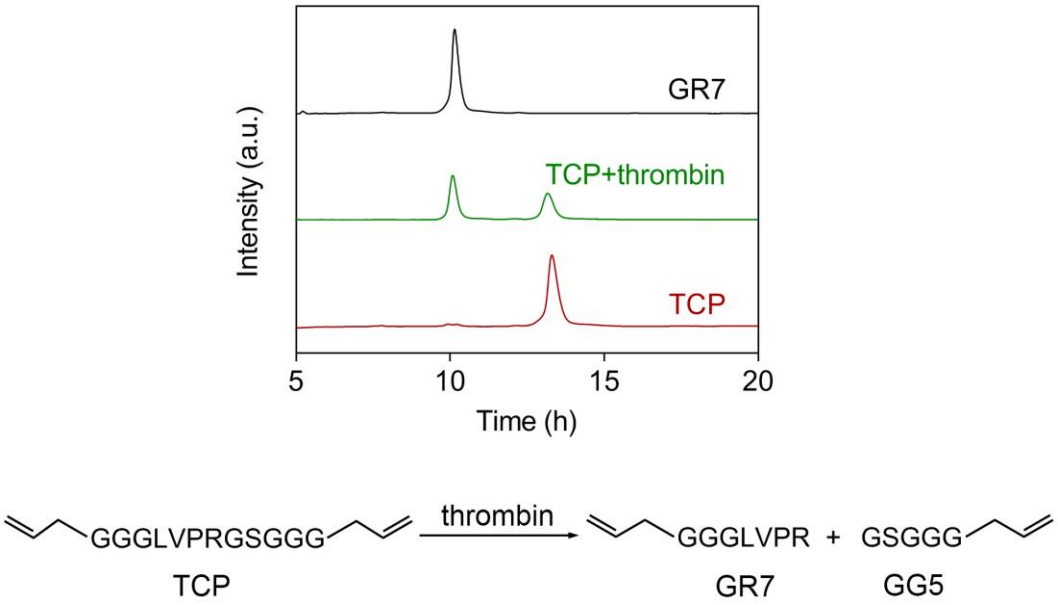

Fig. S2. Representative HPLC profiles of the TCP crosslinker, allyl-GR7 and the thrombin-treated TCP crosslinker (TCP+thrombin). TCP was incubated with thrombin (1 U/mL) for 8 h. Degradation route of TCP by thrombin was shown (lower).

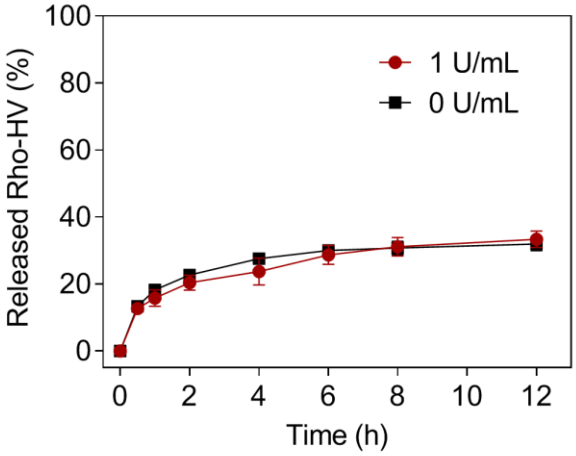

Fig. S3. Release profiles of Rho-HV from Rho-HV/cNGs after incubation with thrombin (1 U/mL) over time. Data are shown as mean ± s.d. (*n* = 3).

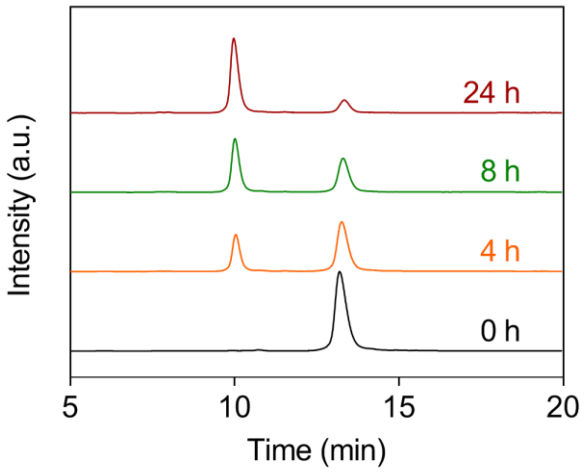

Fig. S4. Representative HPLC profiles of the TCP crosslinker after incubation with thrombin in the presence of heparin for different time.

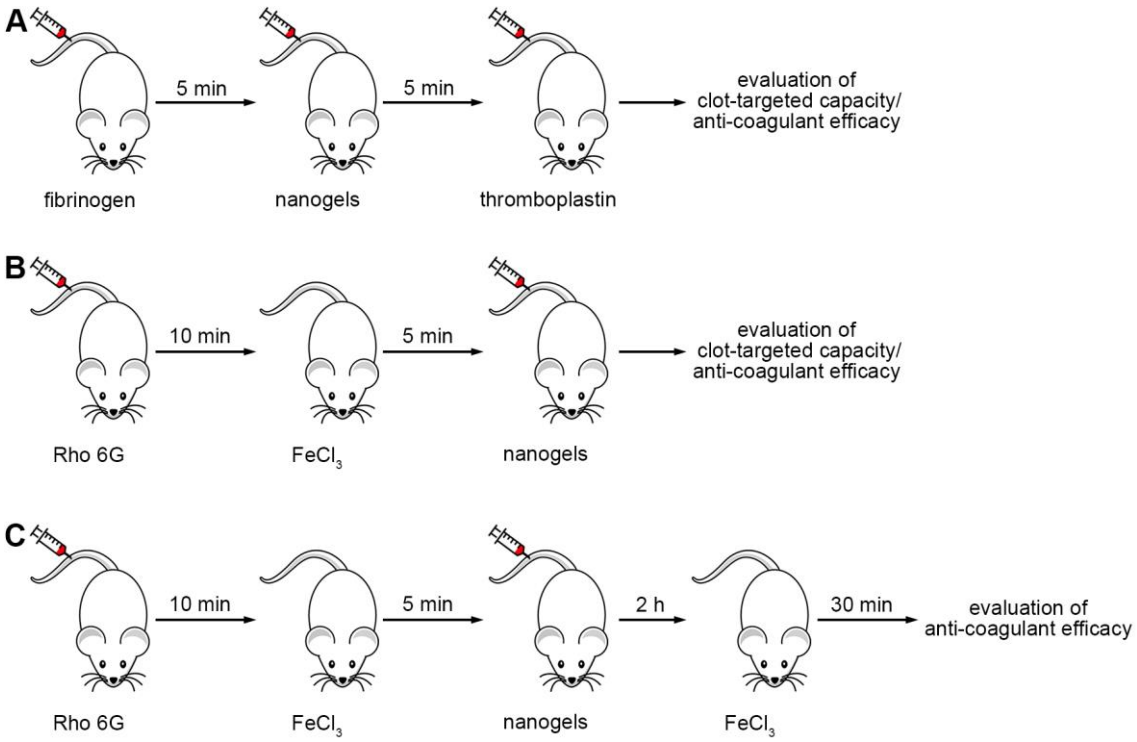

Fig. S5. Schematic illustration of *in vivo* experimental schedules on the mouse models. (**A**) Thromboplastin-induced pulmonary embolism mouse model. (**B**) $FeCl_3$-induced carotid arterial and mesenteric thrombosis models. (**C**) Sequential $FeCl_3$-induced carotid arterial and mesenteric thrombosis models.

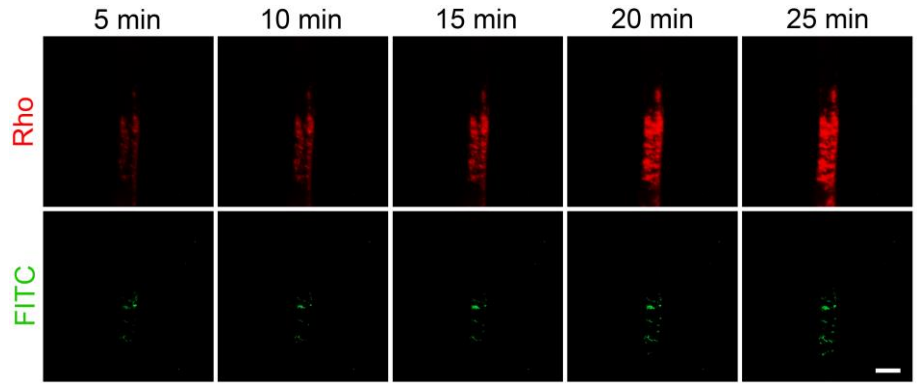

Fig. S6. Evaluation of the clot-targeted capacity of FITC-BSA/tNGs on the $FeCl_3$-induced carotid arterial thrombosis mouse model. Representative fluorescent images of the carotid arteries of the mice after intravenous injection of FITC-BSA/tNGs over time. The blood clots were labeled with Rho 6G. Scale bar is 500 μm.

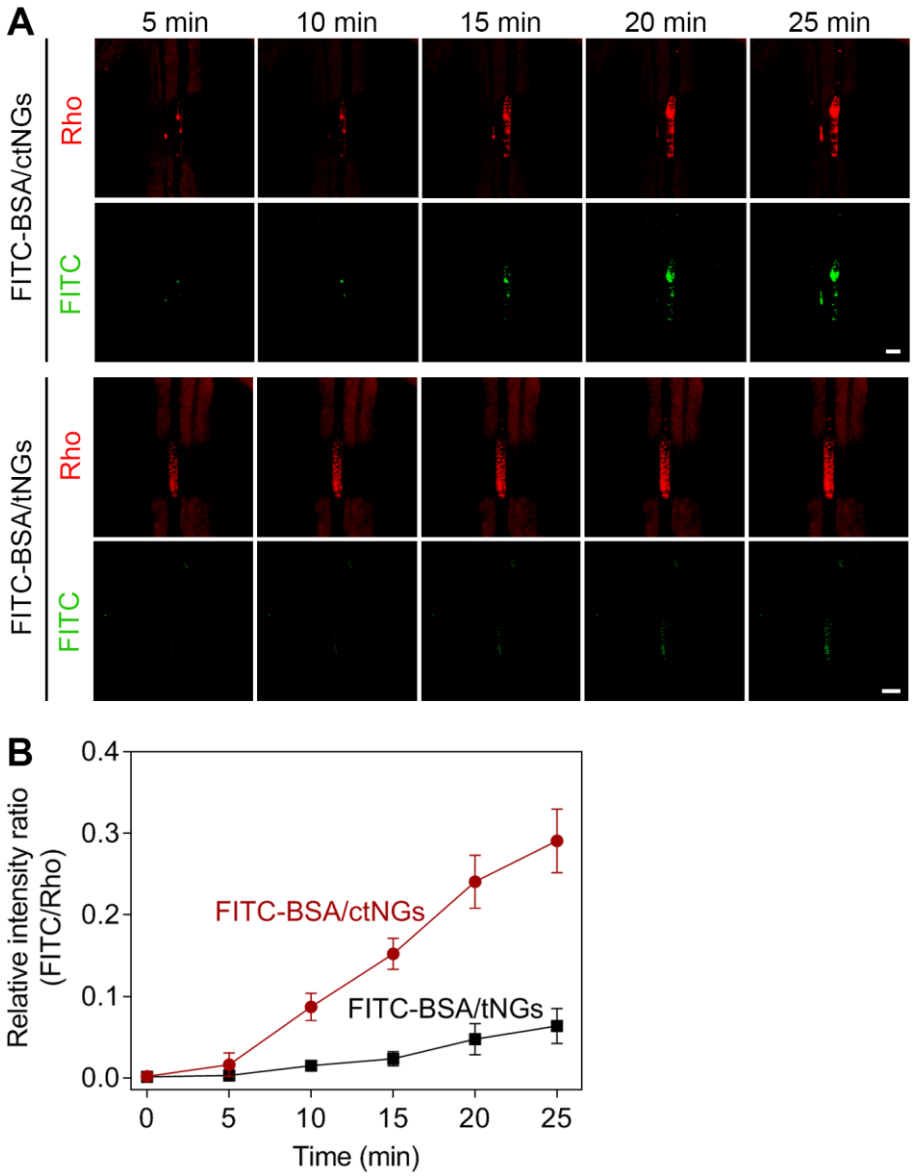

Fig. S7. Evaluation of the clot-targeted capacity of FITC-BSA/ctNGs and FITC-BSA/tNGs on the $FeCl_3$-induced mesenteric thrombosis mouse model. (**A**) Representative fluorescent images of the carotid arteries of the mice after intravenous injection of FITC-BSA/ctNGs and FITC-BSA/tNGs over time. The blood clots were labeled with Rho 6G. Scale bars are 500 μm. (**B**) Changes in the relative fluorescent intensity ratio of FITC to Rho after intravenous injection of FITC-BSA/ctNGs and FITC-BSA/tNGs over time. Data are shown as mean ± s.d. (n = 3).

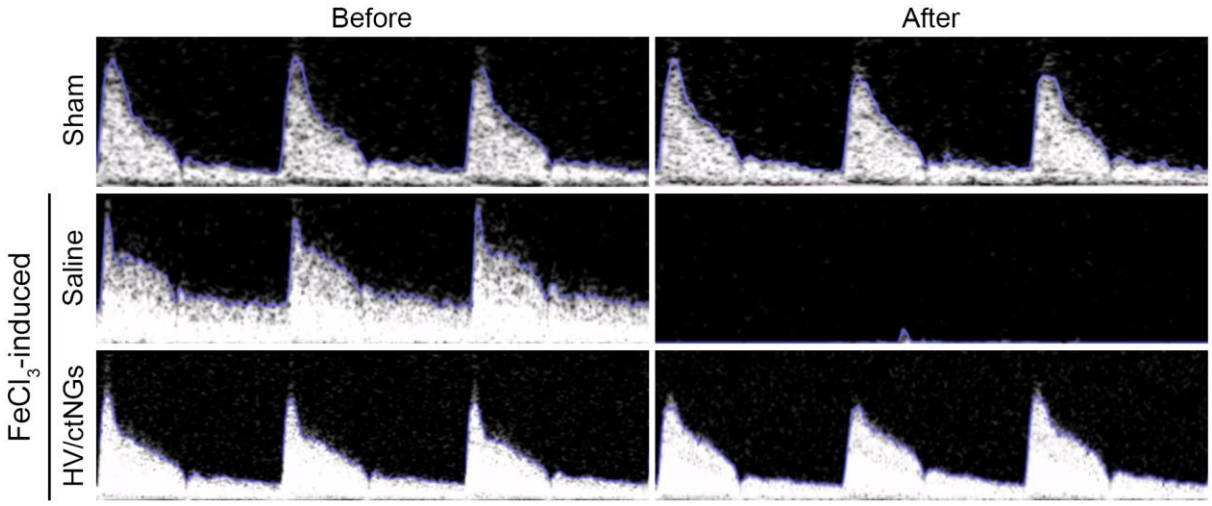

Fig. S8. Pulse wave Doppler images of the carotid arteries of the $FeCl_3$-induced thrombosis mouse model before and after intravenous injection of HV/ctNGs for 25 min.

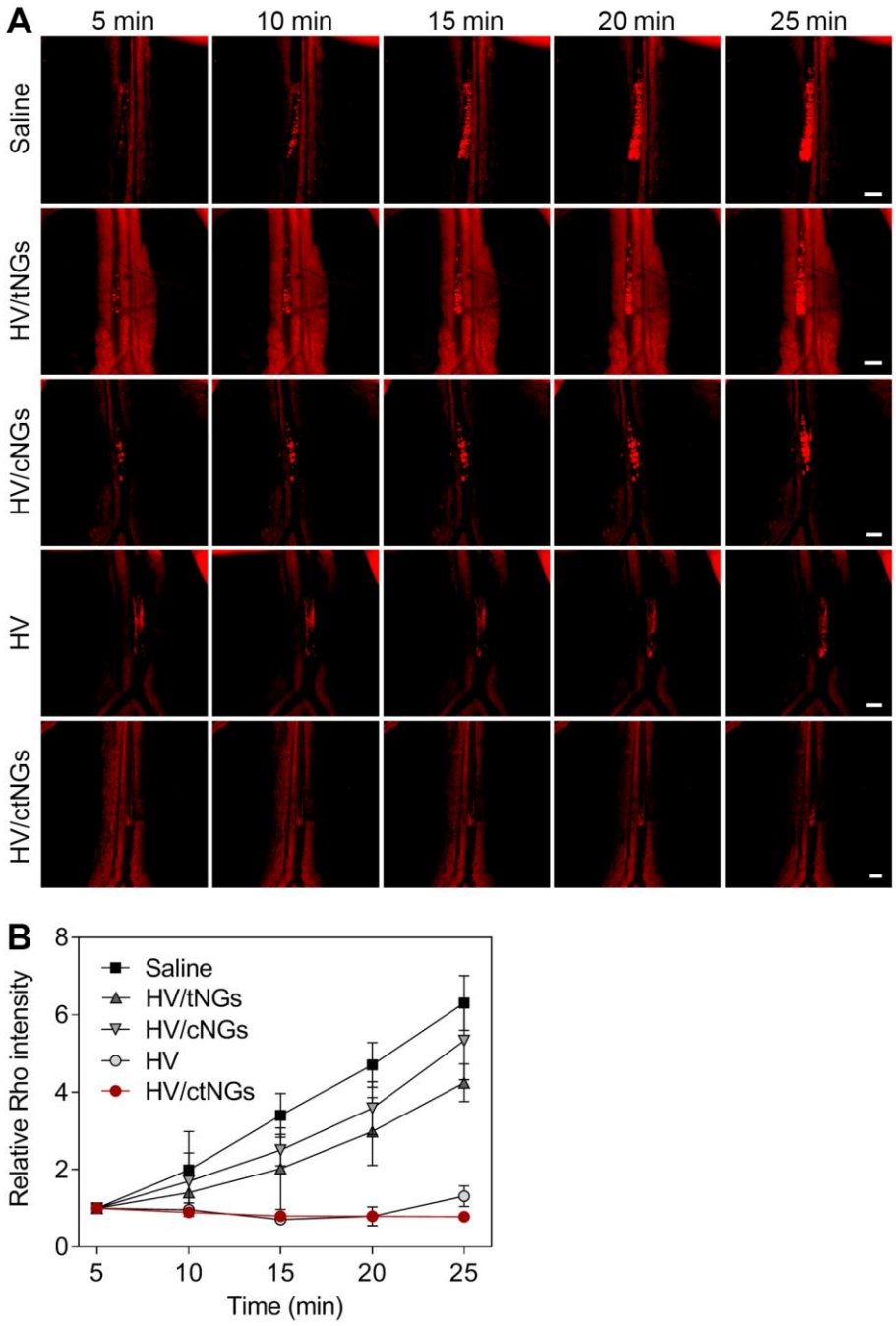

Fig. S9. Evaluation of the therapeutic efficacy of different HV formulations on the $FeCl_3$-induced mesenteric thrombosis mouse model. (**A**) Representative fluorescent images of the mesenteric blood vessels of the mice after intravenous injection of different HV formulations for different time. The blood clots were labeled with Rho 6G. Scale bars are 500 μm. (**B**) Changes in the relative fluorescent intensity of Rho after intravenous injection of different HV formulations over time. Data are shown as mean ± s.d. (n = 3).

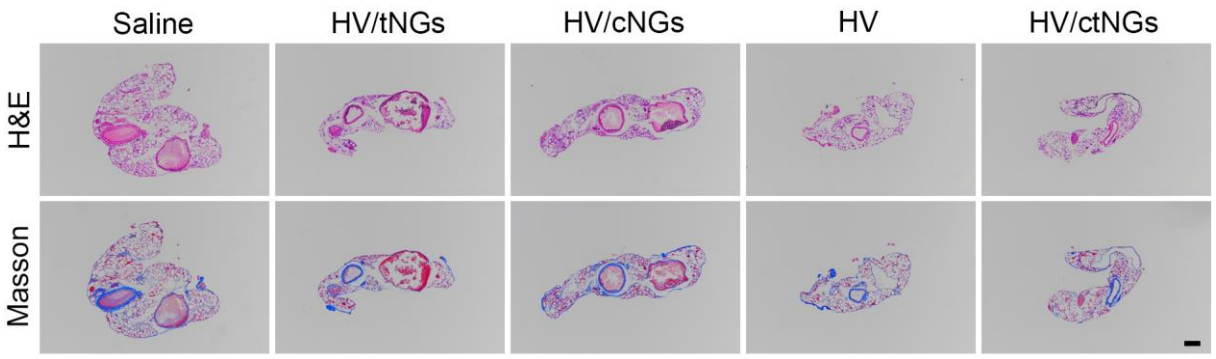

Fig. S10. Representative H&E- and Masson's trichrome-stained images of the blood vessels of the $FeCl_3$-induced mesenteric thrombosis mouse model after different treatments. The blood vessels were examined at 25 min post-injection of different HV formulations. Scale bar is 100 μm.

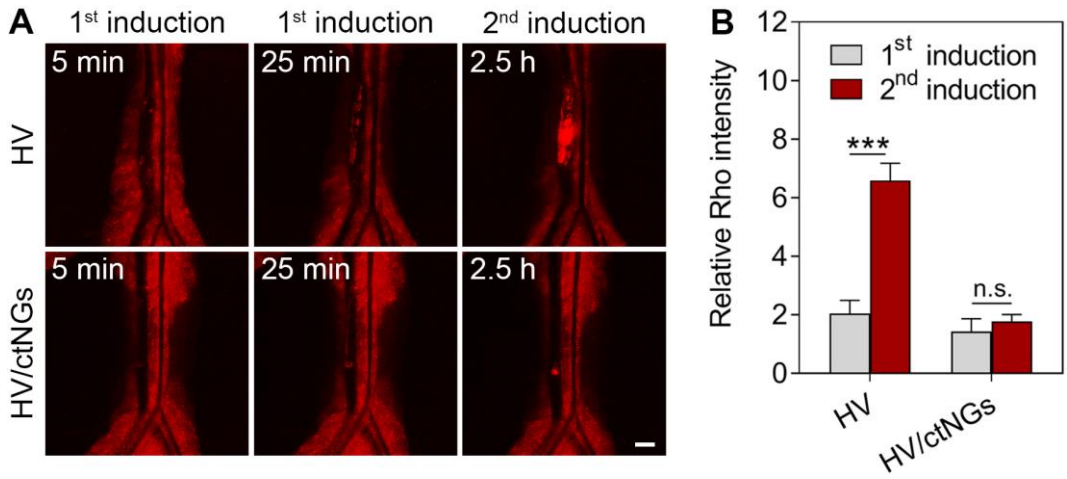

Fig. S11. Evaluation of the therapeutic efficacy of HV and HV/ctNGs on the sequential $FeCl_3$-induced mesenteric thrombosis mouse model. (**A**) Representative fluorescent images of the mesenteric blood vessels of the mice after intravenous injection of HV and HV/ctNGs for different time upon sequential induction. The blood clots were labeled with Rho 6G. Scale bars are 500 μm. (**B**) Relative ratio of the Rho fluorescent signal intensity after intravenous injection of HV and HV/ctNGs upon sequential induction. Data are shown as mean ± s.d. (n = 3). $P > 0.05$ (no significance, n.s.), $^{***}P < 0.001$.

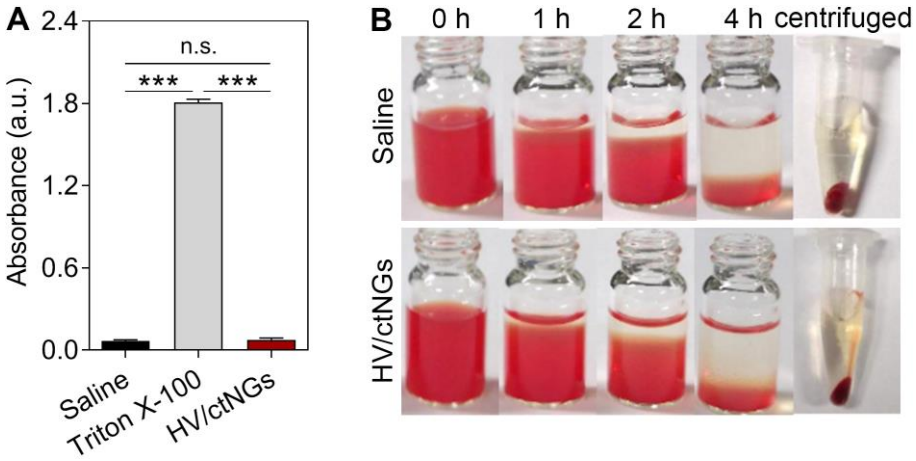

Fig. S12. *In vitro* hemolysis evaluation. (**A**) Absorbance of the supernatant of the mouse RBCs at 570 nm at 4 h post-incubation of HV/ctNGs. Data are shown as mean ± s.d. (n = 3). $P > 0.05$ (no significance, n.s.), $^{***}P < 0.001$. (**B**) Representative images of the RBCs after incubation with HV/ctNGs for different time (Photo Credit: Xiao Xu, Center of Advanced Pharmaceuticals and Biomaterials, China Pharmaceutical University, Nanjing, 210009, China).

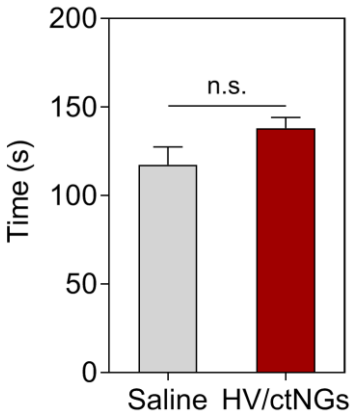

Fig. S13. Bleeding time assay. At 24 h post-injection of HV/ctNGs, a small cut was made on the tail of the mice, and the time was recorded until the bleeding stopped. Data are shown as mean ± s.d. (n = 3). P > 0.05 (no significance, n.s.).

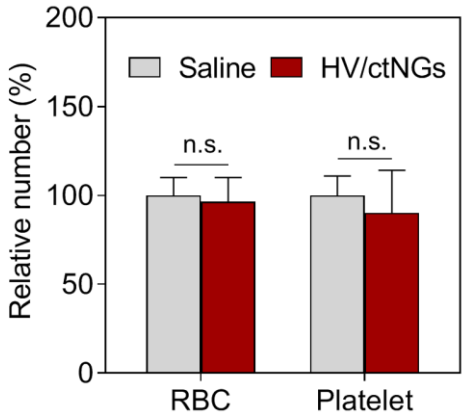

Fig. S14. RBC and platelet count quantification. At 24 h post-injection of HV/ctNGs, the total amounts of RBCs and platelets of the mice were counted. Data are shown as mean ± s.d. (n = 3). P > 0.05 (no significance, n.s.).

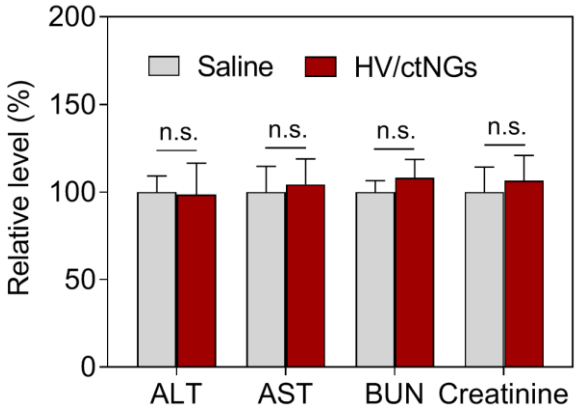

Fig. S15. Liver and kidney function index quantification. At 24 h post-injection of HV/ctNGs, the serum levels of ALT, AST, BUN and creatinine of the mice were determined. Data are shown as mean ± s.d. (n = 3). $P > 0.05$ (no significance, n.s.).

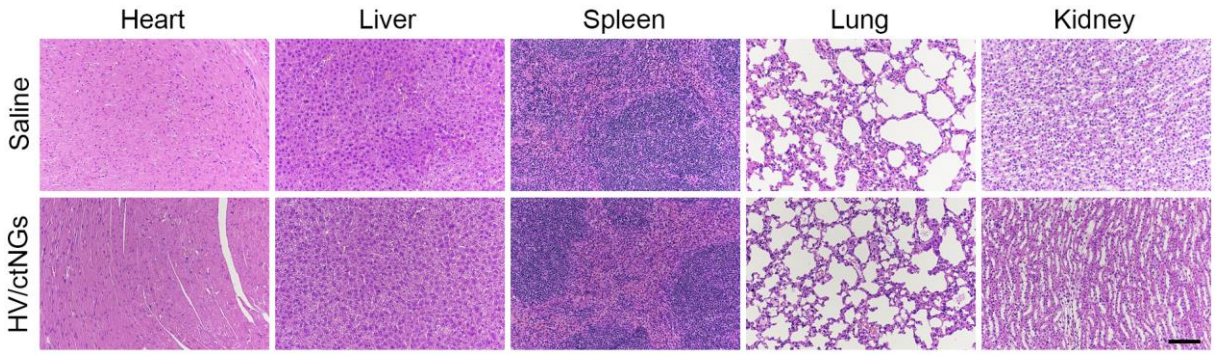

Fig. S16. Histological examination. Representative H&E-stained images of normal tissues of the mice at 24 h post-injection of HV/ctNGs. Scale bar is 100 μm.

Table S1. Particle size, polydispersity index and zeta potential of different NGs. Data are shown as mean ± s.d. (n = 3).

	Particle size (nm)	Polydispersity index (PDI)	Zeta potential (mV)
HV/tNGs	57.4 ± 2.0	0.237 ± 0.025	-1.8 ± 0.4
HV/cNGs	65.4 ± 2.6	0.239 ± 0.023	-2.0 ± 0.5
HV/ctNGs	76.9 ± 1.0	0.228 ± 0.018	-1.2 ± 0.2